

The SAMI Galaxy Survey: The contribution of different kinematic classes to the stellar mass function of nearby galaxies

Kexin Guo,^{1,2*} Luca Cortese,^{2,3} Danail Obreschkow,^{2,3} Barbara Catinella,^{2,3}
 Jesse van de Sande,^{3,4} Scott M. Croom,^{3,4} Sarah Brough,⁵ Sarah Sweet,^{3,6}
 Julia J. Bryant,^{3,4,7} Anne Medling,⁸ Joss Bland-Hawthorn,⁴ Matt Owers,^{9,10}
 Samuel N. Richards¹¹

¹*Kavli Institute for Astronomy and Astrophysics, Peking University, 5 Yiheyuan Road, Haidian District, Beijing 100871, P.R.China*

²*International Centre for Radio Astronomy Research (ICRAR), University of Western Australia, Crawley, WA 6009, Australia*

³*ARC Centre of Excellence for All Sky Astrophysics in 3 Dimensions (ASTRO 3D), Australia*

⁴*Sydney Institute for Astronomy, School of Physics (SfA), A28, The University of Sydney, NSW, 2006, Australia*

⁵*School of Physics, University of New South Wales, NSW 2052, Australia*

⁶*Centre for Astrophysics and Supercomputing, Swinburne University of Technology, PO Box 218, Hawthorn, VIC 3122, Australia*

⁷*Australian Astronomical Optics, AAO-USydney, School of Physics, University of Sydney, NSW 2006, Australia*

⁸*Ritter Astrophysical Research Center, University of Toledo Toledo, OH 43606, USA*

⁹*Department of Physics and Astronomy, Macquarie University, NSW 2109, Australia*

¹⁰*Astronomy, Astrophysics and Astrophotonics Research Centre, Macquarie University, Sydney, NSW 2109, Australia*

¹¹*SOFIA Science Center, USRA, NASA Ames Research Center, Building N232, M/S 232-12, P.O. Box 1, Moffett Field, CA 94035-0001, USA*

Accepted XXX. Received YYY; in original form ZZZ

ABSTRACT

We use the complete Sydney-AAO Multi-object Integral field spectrograph (SAMI) Galaxy Survey to determine the contribution of slow rotators, as well as different types of fast rotators, to the stellar mass function of galaxies in the local Universe. We use stellar kinematics not only to discriminate between fast and slow rotators, but also to distinguish between dynamically cold systems (i.e., consistent with intrinsic axis ratios < 0.3) and systems including a prominent dispersion-supported bulge. We show that fast rotators account for more than 80% of the stellar mass budget of nearby galaxies, confirming that their number density overwhelms that of slow rotators at almost all masses from 10^9 to $10^{11.5} M_{\odot}$. Most importantly, dynamically cold disks contribute to at least 25% of the stellar mass budget of the local Universe, significantly higher than what is estimated from visual morphology alone. For stellar masses up to $10^{10.5} M_{\odot}$, this class makes up $\geq 30\%$ of the galaxy population in each stellar mass bin. The fact that many galaxies that are visually classified as having two-components have stellar spin consistent with dynamically cold disks suggests that the inner component is either rotationally-dominated (e.g., bar, pseudo-bulge) or has little effect on the global stellar kinematics of galaxies.

Key words: galaxies: abundances – galaxies: kinematics and dynamics – galaxies: stellar content

* E-mail: kxguo@pku.edu.cn

1 INTRODUCTION

The stellar mass function (SMF) of galaxies - i.e., the number density of galaxies per unit of stellar mass - has become a key tool for galaxy evolution studies, as its shape and normalization are regulated by the mass assembly history of galaxies (e.g., Macciò et al. 2010; Menci et al. 2012; Kang et al. 2013). With increasing observational data on large samples of galaxies in both the local and the high-redshift Universe, considerable efforts have been made to quantify the overall shape of the SMF for different populations of galaxies as well as its evolution over cosmic time (e.g., Ilbert et al. 2010; Peng et al. 2010; Baldry et al. 2012; Davidzon et al. 2017). This has also made the SMF the primary tool for calibrating cosmological simulations of galaxy formation and evolution (e.g. Genel et al. 2014; Crain et al. 2015; Pillepich et al. 2018).

The analysis of the SMF is even more powerful when applied to different galaxy classes, as it encapsulates the effects of a variety of physical processes on the mass accretion history of galaxies. Thus, it provides important clues on the mass regimes within which different evolutionary paths for galaxy transformation are most likely. For instance, the comparison between SMFs for star-forming galaxies (SFG) and passive galaxies suggests a faster quenching rate in more massive galaxies (e.g., Peng et al. 2010; Ilbert et al. 2010).

Among these studies, the study of SMFs of galaxies of different morphology is a topic of particular interest, as morphological transformation is expected to be intimately tied to galaxy evolution and accretion history. Disc-like structures mostly arise from dissipational gas accretion (e.g., Fall & Efstathiou 1980), while the formation of spheroidal structures, including galaxy bulges and ellipticals, has been widely believed to be related to dissipationless mergers (e.g., Cole et al. 2000). Disk mergers also have an impact in torquing gas to lose the angular momentum in transforming a galaxy from late-type to early-type (e.g., Gerhard 1981; Hernquist 1992, 1993; Heyl et al. 1994).

Several independent works have shown that the mass distribution of late-type (disk-dominated) and early-type (bulge-dominated) galaxies show distinct differences. The early-types dominate at $M_* > 10^{10} M_\odot$, while the late-types dominate at lower stellar mass (Kelvin et al. 2014; Moffett et al. 2016a). Despite this, the two classes contribute nearly equally to the global stellar mass budget of the local Universe, Ω_* (Driver et al. 2007; Moffett et al. 2016b). All these results could implicate that mergers play as important a role in mass assembly as gas accretion, and dominate the galaxy evolution in the massive regime.

The underlying assumption of the above scenario is that visual morphology is able to isolate truly different kinematic components, especially components like dispersion-supported bulges and rotationally-supported disks, which are directly linked to the merging history of galaxies.

While this assumption was commonly accepted in the past, the last decade has clearly shown that galaxies with distinct visual morphology can share similar kinematic properties. Most early-type galaxies (ETGs) are found to have a rotational component (e.g., Kormendy & Bender 1996; Faber et al. 1997; Cappellari et al. 2007; Emsellem et al. 2007, 2011), arguing against the origin of ETGs or massive galaxies as exclusively (dissipationless) mergers. Non-

rotating galaxies, on the other hand, make up only $\leq 1/3$ of the total ETGs, and are found almost only at stellar mass $M_* > 10^{11} M_\odot$ (Cappellari 2016; Brough et al. 2017; Graham et al. 2018).

Therefore, the contribution of the different physical processes to the mass assembly history of galaxies is no longer well understood. While major mergers or multiple minor dry mergers are necessary for the formation of slow rotators (SRs) (e.g., Naab et al. 2014), fast rotators (FRs) can be transformed from late-type disks following a continuous kinematic evolution (Cortese et al. 2016, 2019). Additionally, the bulge component in late-type galaxies can either be a dispersion-dominated classical bulge arisen from galaxy mergers, or a rotating system originated from the secular evolution of disks (Méndez-Abreu et al. 2014; Erwin et al. 2015).

The advent of integral-field spectroscopic (IFS) galaxy surveys is finally helping us to shed some light on this issue, providing a more physically-motivated approach to investigate the assembly history of galaxies. Many works have focused on the relative fraction between FRs and SRs (Cappellari 2016, and references therein), and in most cases limited to pre-visually-classified early-type galaxies.

In this study, we take a different approach and present the first investigation of the contribution of different kinematic families of galaxies to the stellar mass function in the local Universe. In addition to presenting the first stellar mass functions for slow and fast rotators, we split FRs into ‘dynamically cold’ FRs (i.e., consistent with intrinsic axis ratios smaller than ~ 0.3) and ‘composite’ rotators (i.e., either thick disks or bulge-plus-disk objects) to determine their overall contribution to the stellar mass function. This allows us to provide new constraints on the mass-dependent contribution of different physical processes to the whole population of galaxies.

This paper is structured as follows. We introduce the dataset in Section 2 and describe the SMF fitting method in Section 3. We show our results in Section 4 and discuss in Section 5. A Chabrier initial mass function (IMF; Chabrier 2003) is used throughout the paper. We assume the following cosmological parameters: $\Omega_0 = 0.3, \Omega_\Lambda = 0.7, H_0 = 70 \text{ km s}^{-1}$.

2 DATA

Our sample is extracted from the overlap between the SAMI Galaxy Survey internal full data release (v0.11) and the Galaxy and Mass Assembly (GAMA) survey (Driver et al. 2011). The SAMI Galaxy Survey targeted 2153 low-redshift galaxies ($z < 0.1$) in the 3 GAMA equatorial regions corresponding to an area of 144 deg^2 in total, using the SAMI multi-object IFS instrument (Croom et al. 2012) mounted on the 3.9 metre Anglo-Australian Telescope (Bryant et al. 2015). SAMI fibres are fed to the double-beam AAOmega spectrograph (Sharp et al. 2006), providing spectral resolutions of $R = 1812$ for the blue part ($3700 - 5700 \text{ \AA}$), and $R = 4263$ for the red part ($6300 - 7400 \text{ \AA}$) of the spectrum, respectively. The SAMI cubes have $50 \times 50 \times 0.25$ (0.5×0.5) arcsec² spaxels along the spatial direction, covering the 14.7 arcsec diameter aperture of the SAMI hexabundle (Bland-Hawthorn et al. 2011; Bryant et al. 2014) and an average seeing of 2.16 arcsec. The data reduction is described in de-

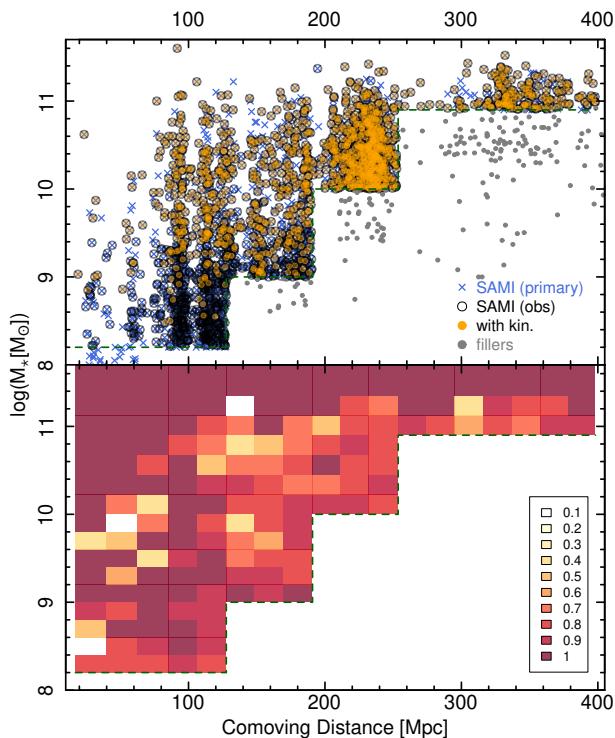


Figure 1. The distribution (*upper*) and the completeness (*lower*) of SAMI(observational) in the stellar mass-comoving distance plane. In the upper panel, the distribution of the SAMI primary sample are labeled as *blue crosses*. All galaxies observed by SAMI are labeled as *black empty circles* (SAMI(observational)), except the filler galaxies (*grey points*). Galaxies with available kinematics in SAMI(observational) are shown as *orange points*. In the lower panel, 1 is assigned to grids with no galaxy in either SAMI(PS) or SAMI(observational) since the fraction-weighted incompleteness correction is not applicable (§3.1).

tail in Allen et al. (2015) and Sharp et al. (2015). We refer readers to Green et al. (2018) and Scott et al. (2018) for Data Releases I and II, respectively.

In this work, we focus on the 1896 galaxies included in the SAMI primary sample (i.e., excluding filler targets), in the footprint of GAMA as described in Bryant et al. (2015), and with a lower-limit mass cut at $M_* > 10^{8.2} M_\odot$ (hereafter “SAMI(observational)”, *black empty circles* in Figure 1)¹. As described in Bryant et al. (2015), the configuration of SAMI plates is done to maximize the number of objects observable within a SAMI field of view, without pre-selection on morphology or environment. The stellar mass estimation is described in Bryant et al. (2015), following the spectral energy distribution (SED) fitting method of Taylor et al. (2011). The uncertainty introduced by photometric error is around 0.05 dex,

¹ We decide to remove 45 galaxies with stellar mass ranging from $10^{7.42}$ to $10^{8.2} M_\odot$ from the original catalog for two reasons. One is that the statistics is low in this relatively large range (~ 0.8 dex). The second is that the SAMI sample selection for $M_* < 10^{8.2} M_\odot$ is not stepwise and the incompleteness is hard to constrain.

while the intrinsic scatter of colour-dependent M/L is about 0.1 dex.

Visual morphology classification in SAMI has been performed taking advantage of Sloan Digital Sky Survey Data Release Nine (SDSS DR9; Ahn et al. 2012) *gri* colour images, as discussed in Cortese et al. (2016). Except for 80 unclassified galaxies (“?” in Figure 4) and galaxies without a consensus in morphology classification (“NA”), 1816 galaxies have classifications from late-type disks to ellipticals without ambiguity. Briefly, galaxies with early-type morphologies (round and smooth) or no presence of spiral arms are classified as ETGs, and the galaxies fulfilling these conditions but having signs of star formation are excluded. ETGs with disks are further classified as S0s. Here, we constrain LTGs to be only visually pure disks/irregular galaxies (late-type spirals, “LS”) and classify other late-type galaxies with intermediate types of morphologies as MTGs. Precisely, LTGs (*blue*) corresponds to “LS” in Figure 4, and MTGs (*greens*) consists of early-or-late-type spirals (“ES/LS”) and early-type spirals (“ES”), with ETGs (*red to yellow*) including all earlier types.

Effective radii (r_e), ellipticities (ϵ), and position angles have been derived using the Multi-Gaussian Expansion (MGE; Emsellem et al. 1994; Cappellari 2002) technique performed on SDSS *r*-band images with the code from Scott et al. (2009) and D’Eugenio et al. (in prep). The MGE method has been performed to fit the observed surface brightness profile in terms of the sum of two-dimensional Gaussians while keeping the position angles of the Gaussians constant and taking the point spread function (PSF) into account. r_e is defined as the semi-major axis effective radius measured from the best MGE fit, and the ellipticity of the galaxy within one r_e is the ϵ used in this study.

Stellar kinematics are measured from the SAMI data by using the penalized pixel fitting code (pPXF, Cappellari & Emsellem 2004; Cappellari 2017) as described in van de Sande et al. (2017a). 1222 Galaxies in the sample have stellar kinematic information (aperture uncorrected) following the criteria of van de Sande et al. (2017b): signal-to-noise $(S/N) > 3 \text{ \AA}^{-1}$, $\sigma_{\text{obs}} > \text{FWHM}_{\text{intr}}/2 \sim 35 \text{ km s}^{-1}$, and $\sigma_{\text{error}} < \sigma_{\text{obs}} * 0.1 + 25 \text{ km s}^{-1}$ (see van de Sande et al. 2017a)². No additional cut on stellar mass or morphology or other kinematic features is applied. The spin parameter within one r_e , λ_{r_e} for each galaxy has been calculated based on Emsellem et al. (2007, 2011), according to Equation 9 in Cortese et al. (2016):

$$\lambda_R \equiv \frac{\langle R|V| \rangle}{\langle R\sqrt{V^2 + \sigma^2} \rangle} = \frac{\sum_{k=1}^n F_k R_k |V_{k \text{ los}}|}{\sum_{k=1}^n F_k R_k \sqrt{V_{k \text{ los}}^2 + \sigma_k^2}}, \quad (1)$$

where n includes all pixels within r_e .

To summarize, we focus on 1896 galaxies observed and selected (“SAMI(observational)”) in total, of which 1816 have certain morphologies from late to early type, and 1222 have kinematic information.

² Only 28 galaxies have $r_e < \text{HWHM}_{\text{PSF}}$ and removing them does not affect our results.

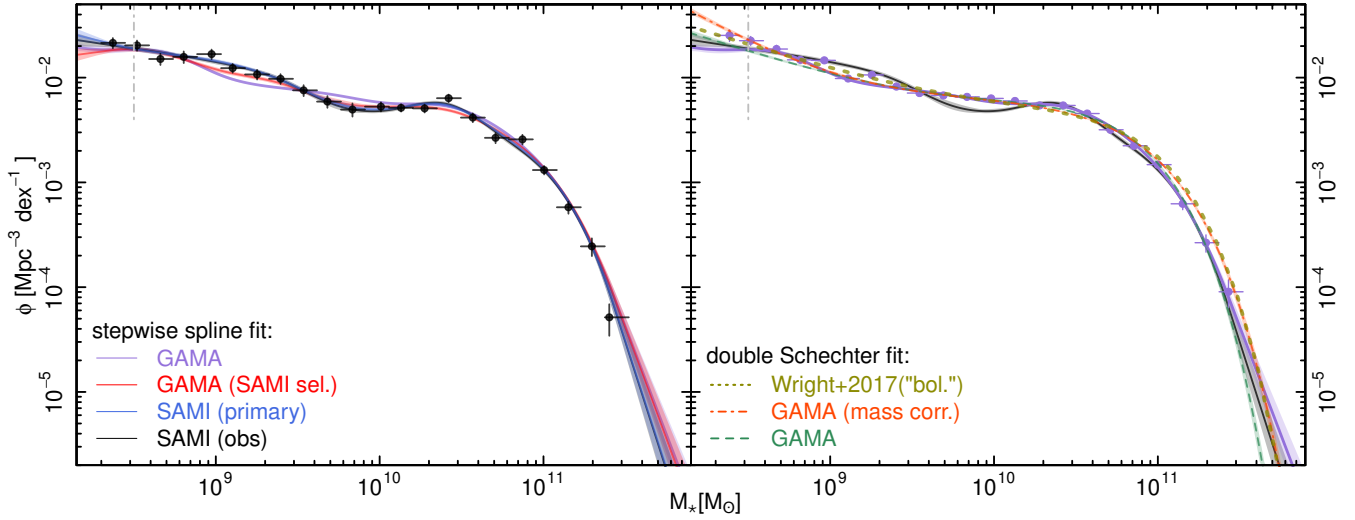


Figure 2. The comparison of the SMFs for GAMA and SAMI galaxies obtained using different sample selections and fitting techniques. *Left:* The coloured lines show the SMF obtained using a stepwise function for SAMI(obs) (*black*), the GAMA-I sample defined in §3 (*purple*), a SAMI-like selection applied to the GAMA-I sample (*red*) and the SAMI primary sample. The *black points* show the SAMI (obs) SMF per bin of stellar mass. *Right:* The SMFs obtained from fitting a double-Schechter functions for the GAMA-I sample with and without aperture corrections applied to the stellar mass (*red* and *green*) and the SMF from Wright et al. (2017) based on the GAMA sample with MAGPHYS stellar masses (*dotted olive line*). For comparison, the step-wise fits for SAMI(obs) and GAMA-I are overplotted in *black* and *purple*. The *purple points* show the GAMA-I SMF per bin of stellar mass. In both panels, the vertical *grey dash-dotted lines* show the lower limit adopted for estimating Ω_* (see text for more details). The consistency between the *solid black line* and the SMFs obtained using different sample selections and/or fitting techniques confirms the reliability of our method and incompleteness correction.

3 METHOD

To derive the SMFs for our sample we use the fitting tool ‘dftools’ (Obreschcow et al. 2018). ‘dftools’ provides maximum-likelihood fitting with both Schechter (Schechter 1976) and stepwise (either linear or spline) functions, with over/under-density estimated and corrected automatically and iteratively. Similar to other SMF fitting methods, the package estimates an effective volume for each grid of M_* , based on a selection function describing the ratio between the number of galaxies accounted into the fitting and that in the real Universe, at given M_* and redshift. However, since the SAMI galaxies are selected from the GAMA I survey which consists of 3 different fields (G09, G12 and G15), the over/under-density correction does not only depend on redshift but also deviates from field to field. Thus, the maximum volume that a galaxy can be observed after density correction (effective volume V_{eff}) at given stellar mass is different from field to field. To address this complication, instead of running the fitting procedure over the full sample, we calculate the effective volume for individual galaxies and incorporate them directly into the fitting. In this section, we describe our method of correcting for the density inhomogeneity and the incompleteness of the sample. We also compare the SMF derived based on this method with that from a volume-limited sample and that from previous works.

3.1 A grid-based V_{eff} method

Although ‘dftools’ fits SMFs to datasets without binning the data, we evaluate the effective volume as a function of stellar mass and cosmic distance on a fine grid (0.2 dex \times 19 Mpc cells) for practical convenience. We adopt the calculation of effective volume in Baldry et al. (2012), which is equivalent to the density-corrected V'_{max} method in Cole (2011). Practically, we select galaxies in the GAMA-I DR2 catalogue (Liske et al. 2015) with $M_* > 10^{9.6} M_{\odot}$ (corresponding to $M_r < -18$ mag) as the density-defining population (DDP), and the effective volume for each galaxy i is given by:

$$V_{\text{eff},i} = \frac{\rho_{\text{ddp}}(0.004; z_{\text{max},i})}{\rho_{\text{ddp}}(0.004; 0.095)}, \quad (2)$$

where $\rho_{\text{ddp}}(z_a; z_b)$ is the number density of DDP between redshift z_a and z_b , and 0.004 and 0.095 are lower and upper redshift limits for SAMI galaxies. Given SAMI’s stepped sample selection (Figure 1), $z_{\text{max},i}$ is one of [0.004, 0.02, 0.03, 0.045, 0.06, 0.095]. It should be noted that, to recover the under-densities and cosmic variance of low-redshift GAMA regions (Driver et al. 2011), we scale our derived SMFs up by a factor of 1.13. This factor is applied to match the integrated number density of galaxies with $M_* > 10^{10} M_{\odot}$ with that calculated based on GAMA galaxies in the same mass range within $0.07 < z < 0.19$, the value of which is also adopted as the fiducial density in Wright et al. (2017).

Besides the galaxy distribution in real space, the incompleteness of the observations is an additional factor that

needs to be accounted for. The simple approach that we apply is to modify the effective volumes in grids of mass and comoving distance by multiplying the original $V_{\text{eff},i}$ by a completeness factor, described by the fraction of galaxies observed in each grid, i.e., $\frac{N_{\text{obs}}}{N_{\text{PS}}}$, where N_{obs} and N_{PS} are the number of galaxies observed and that in SAMI primary sample, respectively. No correction is applied to grids with no galaxy in either sample. The distribution of the completeness factor is shown together with the stepwise-selected SAMI galaxies in Figure 1. The resulting SMF fitted based on the SAMI (obs) sample (*black*) is shown together with that of the SAMI primary sample (*blue*) in Figure 2. The consistency between them for $M_* > 10^{8.5} M_{\odot}$ suggests that the error in grid-based incompleteness correction (Figure 1) is negligible.

To assess the reliability of reproducing SMFs based on galaxies selected from an original dataset, we have performed multiple experiments with artificial selection functions, and compared the output SMFs with the one fit from a parent sample, which consists of galaxies between $0.004 < z < 0.095$ with $\log(M_*/M_{\odot}) > 7.6 + 7.7 \times 10^{-3} \cdot (r/\text{Mpc}) - 6.6 \times 10^{-6} \cdot (r/\text{Mpc})^2$ in the GAMA-I DR2 catalog (Taylor et al. 2011). The above criterion is defined from a binomial fitting to the peak value in the distribution of M_* as a function of comoving distance r . We find that a stepwise-spline function with a ‘reasonable’ step width³ works better than a (double) Schechter function in reproducing SMFs. That is because a stepwise-spline function is a non-parametric model (in the limit of small enough steps) that is more generic than Schechter functions, for which there is no straightforward justification when considering sub-populations of galaxies.

In Figure 2, we show the comparison between the SMF fitted by double Schechter function based on the GAMA parent sample (*right panel, green dashed*), and the SMF fitted by step-wise functions based on the same sample (*purple solid*). The difference between the two is $< 1\%$ in both number and mass density for galaxies with $M_* > 10^{8.2} M_{\odot}$. The SMF fitted by step-wise functions based on GAMA galaxies selected according to the same step-series selection criteria of SAMI primary sample (“GAMA(SAMI sel.)”, *red*) is also plotted. The differences between the GAMA(SAMI sel.) SMF and the former two GAMA SMFs are both $< 2\%$ (6%) in number (mass) density at the same mass range. This error from the stepwise selection is numerically smaller than the 1σ uncertainty of fitting (note that this is not an indication of overfitting since errors can be correlated between different mass bins).

The stellar mass estimations adopted by the SAMI and GAMA surveys are slightly different, with the former based on a $g-i$ colour dependent M_*/M_i (Bryant et al. 2015), approximating the spectral energy distribution (SED) fitting method of Taylor et al. (2011) that have been applied to the latter. The resulting difference in SMF fitting, between SAMI primary sample (“SAMI(primary)”, *blue*) and GAMA galaxies selected by SAMI selection criteria (*red*), can also be found in the left panel of Figure 2. The two SMFs match

³ For example, the width should not be smaller than 0.1 dex in fitting a SMF based on 300 galaxies ranging from 10^9 to $10^{12} M_{\odot}$. In practice, we adopt a step width of 0.34 dex to make sure that every step contains > 25 galaxies.

each other very well ($< 2\%$ in both number and mass density) for $M_* > 10^{9.5} M_{\odot}$, and the deviation for the less massive part causes an offset of 8% in number density but less than 1% in mass density, which is very small compared to other uncertainties contributed by selection function and fitting errors.

Correction of Eddington bias (Eddington 1913) is a built-in procedure in ‘dftools’. However, given the low level of random noise (~ 0.05 dex) in stellar mass estimation propagated from the photometric error, the uncertainty in fitting parameters caused by not considering Eddington bias is small relative to that of the fitting itself, which is estimated by Laplace approximation, equivalent to performing bootstrap iterations of resampling in most cases (for details, see Obreschkow et al. 2018).

We find a total value of $\Omega_* = 1.41 \pm 0.10_{-0.29}^{+0.36} \times 10^{-3}$ relative to the critical density, calculated by integrating the mass density of galaxies with $10^{8.5} < M_*/M_{\odot} < 10^{12}$, where the second uncertainty components come from the systematic uncertainty of 0.1 dex on stellar mass estimation based on g - and i -band photometry (Taylor et al. 2011). The difference caused by not applying aperture correction for stellar mass estimation (*green dashed* vs. *orange dash-dotted*) in the right panel of Figure 2) is $\sim 4.4\%$ in this mass range. Given the value of $\Omega_* = 1.61 \times 10^{-3}$ by integrating the “bolometric” SMF of Wright et al. (2017) in the same mass range, the difference between our value and that from other works (Wright et al. 2017, and references therein) can mostly be explained by the difference in sample selection and fitting methods.

To summarize, despite the marginal difference caused by using different stellar mass catalogues, the reliability of our method in correcting the selection function and other incompleteness has been demonstrated by the consistency between the SMF estimated based on the GAMA-I sample and that of galaxies observed by SAMI. Given that our main goal is to compare SMFs and contributions to Ω_* for different types of galaxies (i.e., relative differences), small systematic effects in the normalisation do not significantly affect our main conclusions.

3.2 An application on stepwise SMFs divided by morphology

We apply the grid-based V_{eff} method described above in deriving SMFs divided by morphology. Morphological types are defined in the previous section, and include ETGs (ellipticals and S0s), MTGs (mainly early spirals), and LTGs (late spirals). The fraction of galaxies that are morphologically classified is higher than 97%. Practically, we correct this incompleteness by weighting V_{eff} by the fraction of galaxies with certain morphologies in grids defined in §3.1. Only marginal differences would be found if no correction was applied.

We show our fitting curves together with the weighted number density in Figure 3, with coloured regions showing 1σ error of the best-fit curve. Consistent with what has been found in statistical studies based on visually-classified morphology (e.g., Kelvin et al. 2014; Moffett et al. 2016a), from low to high stellar masses, the morphology of galaxies becomes more and more spheroidal, with a transition mass between disk-dominated and spheroid-dominated galaxies at

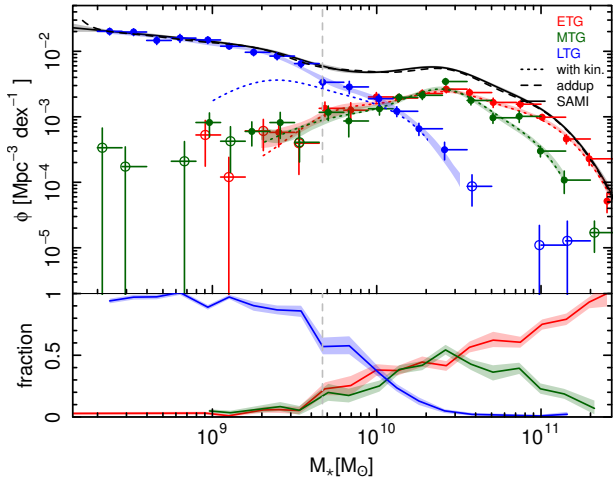


Figure 3. *Upper panel:* The SMFs for all our SAMI observed sample (*black solid line*), and for individual classes of visual morphology (from ETG in red to LTG in blue). We show the best-fitting function for bins with more than 4 galaxies. The *dotted lines* show how the result would change if we included only galaxies with available kinematic information. The sum of the SMFs of all fitting curves is shown by the *black dashed line*. *Lower panel:* The fraction in the number density of different classes at given stellar mass. The *vertical dashed line* shows the completeness limit in stellar mass when comparing galaxies of different kinematic type, same as that in Figure 5b. Our SMFs for different morphological classes are qualitatively consistent with previous works.

around $10^{10}M_{\odot}$. It is hard to give a quantitative comparison with other studies, given the different techniques/datasets used to perform visual classification. However, our results qualitatively agree with the SMFs of “Spheroid Dominated” and that of “Disc Dominated” in Kelvin et al. (2014) and Moffett et al. (2016a) if LS and ES/LS labeled in Figure 4 are taken as “Disc Dominated” galaxies.

4 SMF DIVIDED BY KINEMATIC TYPES

In this section, we focus on the SMF as a function of kinematic classes to explore the mass budget of each kinematic type to the whole galaxy population. This can allow us to gain insights into the different physical processes responsible for (re)shaping the stellar orbits during the assembly history of galaxies. We use the spin parameter (λ_{r_e}) and ellipticity (ϵ) plane to define different families of objects. We adopt the separation between FRs and SRs from Cappellari (2016) (*black frame* in Figure 4), and we consider galaxies without available kinematic information (i.e., observed by SAMI but not fulfilling the quality cuts for stellar kinematic, “nokin”) as a separate type.

In order to distinguish FRs with low and high spin at fixed ellipticity, which we refer to “FR–” and “FR+”, respectively, we use the predicted relation presented by Binney (2005, see also Equation 14–16 in Cappellari 2016). In particular, given that the anisotropy of a FR is bounded by a relation of the form $\delta \approx \beta_z = 0.7 \times \epsilon_{\text{intr}}$ (Cappellari et

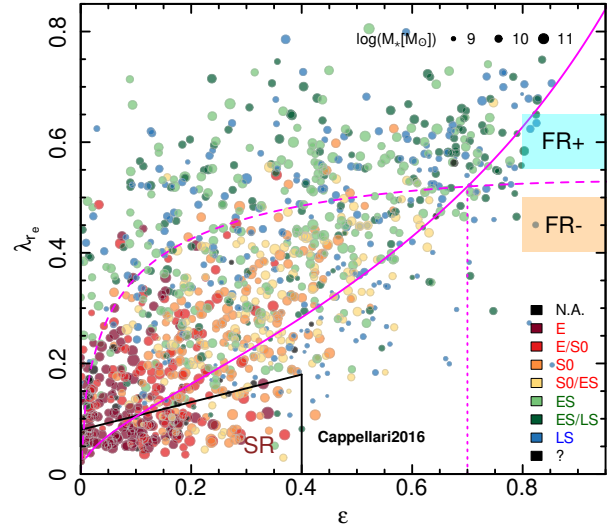


Figure 4. The distribution of spin parameter (λ_{r_e}) and ellipticity (ϵ) for the 1222 galaxies with reliable kinematic information. Galaxies are coded by morphological type in colour and stellar mass in size. The *black frame* on the bottom left shows the separation between fast and slow rotators defined by Cappellari (2016), while the *solid magenta line* shows the theoretical prediction for the edge-on view of galaxies with constant anisotropic factor $\delta = 0.7 \times \epsilon_{\text{intr}}$ (Cappellari et al. 2007). A galaxy with $\epsilon_{\text{intr}} = 0.7$ viewed from different inclination angles outlines the segment between ϵ of 0 and 0.7 on the *magenta dashed line*, which is selected to be the separation between FR+s and FR–s.

al. 2007), FRs with λ_{r_e} higher than predicted at a given ϵ_{intr} are more isotropic than those below such a threshold⁴. Thus, we use a value of $\epsilon_{\text{intr}} = 1 - 0.3 = 0.7$ (*dashed magenta line* in Figure 4) to divide ‘dynamically cold’ systems (FR+) from slower axis-symmetric rotators (FR–). This is equivalent to assuming an ideal model of a galaxy with intrinsic ϵ of 0.7 and viewing it from different inclination angles. The separation line then corresponds to the different projections, according to Equation 12 in Cappellari et al. (2007, see also Binney & Tremaine 1987, Section 4.3). This cut is roughly consistent with the typical threshold separating visually late-type spirals from composite systems and/or bulges (see also Weijmans et al. 2014; Foster et al. 2017)

The plane used for our kinematic selection is shown in Figure 4, with morphological types shown in different colours. Besides a general trend from late-type dominant to early-type dominant with decreasing λ_{r_e} , it is also evident that FRs consists of all morphological types, while SRs are mainly ellipticals or S0s with stellar mass greater than

⁴ For a detailed calculation, see Equation B1 in Emsellem et al. (2007) and Equation 12–16 in Cappellari et al. (2007). We adopt $\kappa = 1$ as the conversion factor between V/σ and λ_R . The changing of κ value from 0.97 (van de Sande et al. 2017b) to 1.1 does not affect our conclusion, simply shifting the mass fraction of 4% from FR+ to FR– if the same ϵ_{intr} cut is adopted.

$10^{11}M_{\odot}$. This minority and mass preference of SRs is consistent with previous works focusing on fractions of galaxies with different kinematics (e.g., Brough et al. 2017; van de Sande et al. 2017b; Graham et al. 2018), and a larger portion of the mass budget from FRs compared to SRs is also expected.

In Figure 5, we compare the incompleteness-corrected SMFs for all FRs and SRs (a), and for the three kinematic classes selected above (FR+, FR-, SR). The SMF for galaxies without kinematic information are plotted as *grey* lines. Due to the small number statistics of SRs, which causes the fit not make much physical sense, we show only number densities for SRs. The fraction of each population at given stellar mass is also shown in lower panels.

From Figure 5a, it is clear that the number density of FRs overwhelms SRs for most stellar masses covered by SAMI, with SRs matching the fraction of FRs only at $> 2 \times 10^{11}M_{\odot}$ (see also Khochfar et al. 2011; Emsellem et al. 2011; Greene et al. 2017, 2018; van de Sande et al. 2017b; Brough et al. 2017). We should note that this transition mass looks systematically lower than that found in Graham et al. (2018, Figure 13) based on MaNGA galaxies. It is plausibly because we assume a unified Chabrier IMF for all galaxies throughout the study, which may lead to an underestimate of stellar mass for massive dispersion-dominated galaxies (Cappellari et al. 2012). Nevertheless, conversely to what is observed in the case of visual morphology between late- and early-type galaxies, there is no apparent transition point in population dominance between FR and SR classes below $10^{11.3}M_{\odot}$. This difference results from the broad overlap in kinematic properties between galaxies with different morphological type, which can already be seen from Figure 4.

This difference between morphological and kinematic classification is even more dramatic if we determine the contribution of different kinematic classes to Ω_* by integrating the SMF for different classes for $M_* > 10^{9.7}M_{\odot}$, which roughly corresponds to the stellar mass at which our completeness in stellar kinematics drops below $\sim 80\%$. We find that $\sim 82\%$ of the stellar mass in the local Universe is hosted in FRs, whereas only $\sim 14\%$ is harboured in SRs, the remaining $\sim 7\%$ is hosted in galaxies for which a kinematic classification was not possible.

As shown in Figure 5a, the fraction of galaxies with no kinematic information increases with decreasing stellar mass, and practically dominates our sample below $M_* \sim 10^{9.5}M_{\odot}$. This makes it unclear whether FRs dominate the whole galaxy population down to the low-mass end. To push the constraint of the ratio of FRs to SRs down to 10^9M_{\odot} , we introduce the assumption that low-mass SFGs should be FRs. This is based on the expectation that star formation takes place in disks and it is supported by the fact that SRs are expected to be produced mainly by gas-poor mergers (e.g., Lagos et al. 2018a,b) and hosted by low specific-star-formation-rate (sSFR) galaxies (Naab et al. 2014). Moreover, star-forming galaxies at this low-mass end are known to have relatively high angular momentum compared to their baryonic mass (Butler et al. 2017).

Specifically, we assume galaxies with $\Delta(\text{SFR}) = \text{SFR} - \text{SFR}_{\text{MS}} > -1$ dex to be FRs, where SFR is star formation rate taken from the multi-wavelength observation based MAGPHYS catalog (Davies et al. 2016;

Table 1. The percentage of the mass budget for different classes of kinematics for galaxies. Comparisons are presented for the same galaxies with seeing correction applied based on Graham et al. (2018).

$f_{\Omega_*}(M_* > 10^{9.7}M_{\odot})$	FR	FR+	FR-	SR	nokin
original (this work) (<i>solid</i> in Figure 5a)	82%	27%	55%	14%	4%
with seeing correction (FR) of Graham et al. (2018)	82%	57%	25%	14%	4%
with seeing correction (all) of Graham et al. (2018)	88%	57%	31%	8%	4%
$f_{\Omega_*}(M_* > 10^9M_{\odot})$					
original	79%	-	-	14%	7%
with FRs complemented (<i>dashed</i> in Figure 5a)	84%	-	-	14%	2%

Driver et al. 2018), and SFR_{MS} are for galaxies on the star formation main sequence (SFMS) defined by a broken linear power law approximation⁵. The effect of this correction to the SMFs and relative fraction of FRs in our sample is shown by the blue dashed lines in Figure 5a. As expected, the fraction of FRs becomes flat down to 10^9M_{\odot} , and contribution of FRs to the stellar mass budget of the local Universe increases to 84%.

In Figure 5b, we present the SMFs and relative fractions obtained by splitting FRs into two different kinematic classes as described above. These two classes show a similar stellar mass distribution, with FR- clearly dominating in number for $M_* > 10^{10.2}M_{\odot}$. It is less clear what happens for $M_* < 10^{9.7}M_{\odot}$: while FR- seem to still be the dominant population until $10^{9.5}M_{\odot}$, the number of galaxies with no kinematic information becomes significant and we cannot exclude that the decrease in the SMFs of FR+ is simply an incompleteness effect. Regardless, by integrating the SMFs of the two classes we find that FR- harbour nearly a factor of ~ 2 more mass than FR+ (i.e., 55% vs. 27%).

It is interesting to compare visual morphology with kinematic classification. As shown in Figure 5b, at stellar masses where late spirals give way to the early types ($M_* \sim 10^{10}M_{\odot}$), there is still a good fraction of dynamically cold galaxies (FR+) which are generally visually classified as two-component galaxies. This indicates that dynamically cold galaxies defined from their kinematics are much more predominant than their morphological counterpart, i.e., the LTGs.

To test if this conclusion varies with the changing of our separation between FR+ and FR-, we check the ratio of the number of visually classified LTGs (N_{LTG}) and MTGs (N_{MTG}) as a function of stellar mass and the threshold used to define the two classes: i.e., 0.6, 0.7 (this work) and 0.8

⁵ Our SFMS is $\log(\text{SFR}) = 0.99 \log(M_*) - 9.89$ for $M_* < 10^{10}M_{\odot}$, and $\log(\text{SFR}) = 0.23 \log(M_*) - 2.29$ for $M_* \geq 10^{10}M_{\odot}$. This agrees with Guo et al. (2015) and Popesso et al. (2019) in corresponding $M_* - z$ range, and the selection guarantees a fraction of $> 96\%$ galaxies with kinematic information to be FRs.

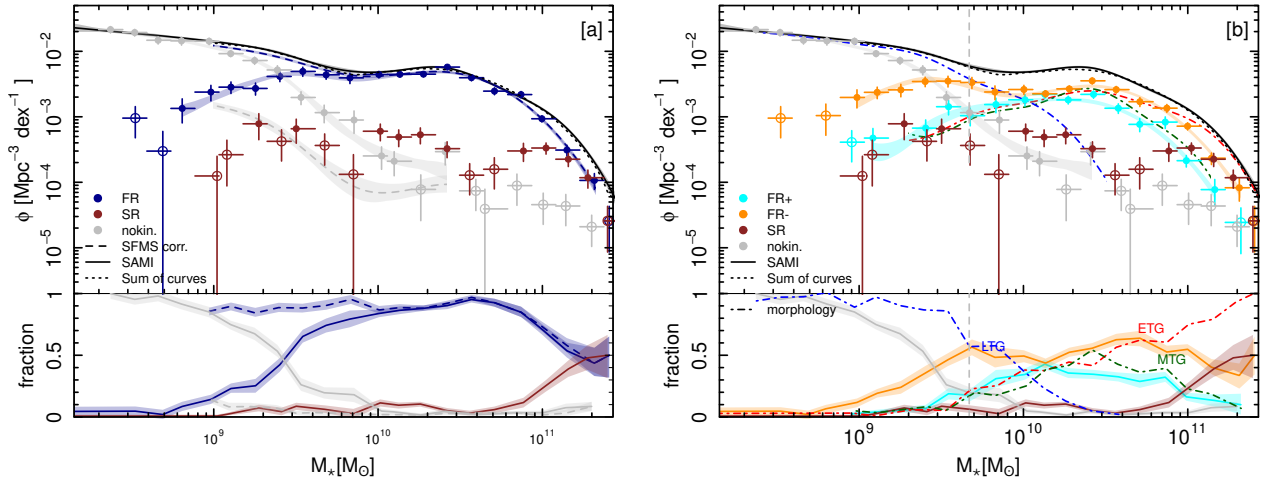


Figure 5. *Left:* SMFs divided by kinematic types for FRs and the number density for SRs. The *solid black* line shows the SMF for the full sample, and *gray* symbols galaxies without available kinematic information. FRs are indicated in blue and SRs in red. As in Figure 3, points are average number density in each mass bin and best-fitting curves shown only for mass bins with more than 4 galaxies. The fraction between populations at given stellar mass (in logarithm) are shown in lower panels. The blue and grey dashed lines in both panels show the change introduced by assuming that all star-forming galaxies with no kinematic information are FRs. *Right:* Same as left panel, but separating FRs+ from FRs-. The fractional distribution of morphological types is also shown for reference. In the right panel, the *vertical dashed line* sets a lower M_* limit above which we can make an unambiguous comparison between populations. FRs dominate the whole galaxy sample until $10^{11}M_{\odot}$ with “warmer” FR-s overwhelming “colder” FR+s at $M_* > 10^{10}M_{\odot}$, and most of massive FR+s are contributed by non-LTG galaxies.

(Figure 6). As expected, FR- are dominated by visually classified MTGs across nearly the entire mass range investigated here ($M_* > 10^{10.2}M_{\odot}$), for stellar masses greater than $\sim 10^{10}M_{\odot}$ the majority of FR+ would be visually classified as MTGs. While the exact value of the ratio $N_{\text{LTG}}/N_{\text{MTG}}$ varies as a function of the threshold used to separate the two kinematic classes, our overall conclusions are not qualitatively affected.

A potential issue affecting our result is the effect of beam smearing on the estimate of λ_{r_e} . This could artificially reduce the value of stellar spin parameter, enhancing the importance of slow rotating systems for the stellar mass budget of the local Universe. To test the potential effect of beam smearing, we apply the Sérsic-index dependent seeing correction presented by [Graham et al. \(2018\)](#). Although, technically, this correction is suitable only for FRs, we also check that our results do not change in case we blindly apply this correction to all our sample. The results are shown in Table 1. While, as expected, the relative contribution of FR and SR to Ω_* is almost independent of any beam smearing effect, the situation is more complicated for the two classes of fast rotators. Once the [Graham et al. \(2018\)](#) correction is applied, the role of FR+ and FR- is reversed, with FR+ galaxies becoming the dominant population. While this would further reinforce our argument that dynamically cold disks are considerably more important than suggested by visual morphology, the change by almost a factor of two in the contribution to Ω_* of different classes of FRs highlights the challenges in interpreting individual estimates of stellar spin at face value.

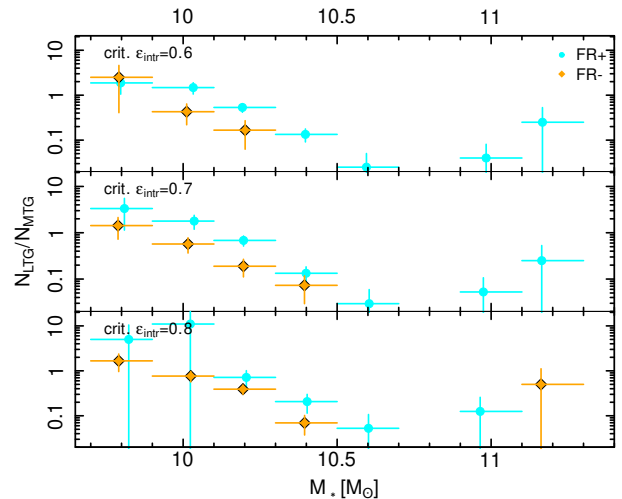


Figure 6. The ratio between the number of LTGs and MTGs as a function of stellar mass in groups of FR+ and FR-, with changing ϵ_{intr} in separating dynamically-cold systems from fast rotators. MTGs always occupy a good fraction of massive FR+s, no matter how “cold” this group is defined to be.

5 DISCUSSION AND CONCLUSION

In this paper, we have tested our ability to accurately reconstruct the SMFs for the SAMI Galaxy Survey, properly taking into account all the selection effects included in

the original sample selection and the observations. We have quantified for the first time the SMFs for galaxies showing different stellar kinematic properties. We confirm that fast rotators (FRs) are the dominant population at almost any stellar mass. FRs contribute $\sim 80\%$ to the total stellar mass budget, with the ratio between FRs and SRs decreasing with increasing stellar mass only for $M_* > 10^{10.5} M_\odot$. At least one-third of the stellar mass harbored by FRs is found in systems with kinematic properties consistent with the thinnest rotating disks, with rotators having low stellar spin starting to dominate at $M_* > 10^{10} M_\odot$. This is clearly in contrast with the equal contribution of spheroidal and disk components to the stellar mass budget of the local Universe as argued from visual morphology studies (Moffett et al. 2016a,b).

In our study, SRs that are believed to be mostly generated from (dissipationless) mergers (e.g., Jesseit et al. 2009; Naab et al. 2014; Lagos et al. 2018b), are confirmed to take up to only $< 20\%$ of the mass density, with most of them found in galaxies with $M_* > 10^{10.5} M_\odot$. This minority suggests that the processes which completely destroy ordered rotation play a small part in the mass assembly of the average galaxy in the local Universe, and only have effect on galaxies with $M_* > 10^{10.5} M_\odot$.

The spin of a regular rotator is intrinsically correlated to its intrinsic ellipticity (Cappellari et al. 2007). Therefore disk thickening and the formation of a classical bulge will cause a decrease in λ_{rc} (e.g. Cappellari et al. 2013; Cappellari 2016, and references therein), making a galaxy move downwards from the group of FR+ to FR- in Figure 4. While the bulge formation could also take place at earlier times than the build-up of disk in the early assembly history of a galaxy (van den Bosch 1998; Lilly & Carollo 2016; Woo, & Ellison 2019, see also van de Sande et al. 2018), nevertheless, the fact that the ratio between FR- and FR+ seems to increase with mass for $M_* > 10^{10} M_\odot$ implies that the processes that efficiently thicken a disk and/or form a classical bulge are mostly efficient in this mass range.

It is also interesting to note that, for $M_* > 10^{10} M_\odot$, the number density of FR+ surpasses that of late-type spirals, with the trend of FR+ fraction with stellar mass similar to that of MTGs (typical two-component galaxies) in morphology. While works based on visual morphology suggest that a stellar mass of $\sim 10^{10} M_\odot$ is a transition mass between bulge- and disk-dominant galaxies, our results seem to imply that many galaxies which are morphologically classified as multiple component systems including a “bulge” are still as dynamically cold as late-type spirals. In other words, a significant fraction of the two-component galaxies are disks when using a global kinematic estimator such as λ_{rc} . The FR+ fraction decreases for stellar masses larger than $\sim 10^{10.5} M_\odot$, most likely because of the increasing emergence of both disk thickening and/or the dissipationless processes creating classical bulges and/or SRs.

Lastly, we remind the reader that our classification of FR+/FR-, i.e., dynamically-cold/two-component disks, is based on the distribution of λ_{rc} as a function of ϵ of galaxies, without applying any kinematic decomposition of the velocity field such as those introduced by Tabor et al. (2017) and Rizzo et al. (2018). The next step for this type of study is to start separating different kinematic components within galaxies and to quantify their contribution to the stellar mass budget in the local Universe. This should provide bet-

ter constraints on the different physical processes regulating the mass growth of galaxies as, at this stage, we are sensitive only to processes significantly perturbing the global stellar velocity fields. Given that both observational (Tabor et al. 2017, 2019; Rizzo et al. 2018) and theoretical (Scannapieco et al. 2010; Martig et al. 2012; Wang et al. 2019; Zhu et al. 2018) works have clearly shown that photometric and kinematic decomposition do not always agree, we cannot blindly rely on 2D bulge-to-disk decomposition if we aim at improving our reconstruction of the accretion histories of nearby galaxies.

ACKNOWLEDGEMENTS

We thank the anonymous referee for their constructive suggestions. We acknowledge the helpful discussions with Dr. Angus Wright. KG acknowledges the support from the Beijing Natural Science Foundation (Youth program) under grant no.1184015. Parts of this research were supported by the Australian Research Council Centre of Excellence for All Sky Astrophysics in 3 Dimensions (ASTRO 3D), through project number CE170100013. LC is the recipient of an Australian Research Council Future Fellowship (FT180100066) funded by the Australian Government. DO acknowledges support by the Australia Research Council Discovery Project 160102235. JvdS is funded under Bland-Hawthorn’s ARC Laureate Fellowship (FL140100278). SB acknowledges the funding support from the Australian Research Council through a Future Fellowship (FT140101166). SS acknowledges the Australian Research Council Centre of Excellence for All Sky Astrophysics in 3 Dimensions (ASTRO 3D), through project number CE170100013. JJB acknowledges support of an Australian Research Council Future Fellowship (FT180100231). JBH is supported by an ARC Laureate Fellowship that funds Jesse van de Sande and an ARC Federation Fellowship that funded the SAMI prototype. MSO acknowledges the funding support from the Australian Research Council through a Future Fellowship (FT140100255). This research is also supported jointly by China National Postdoctoral Science Foundation (No. 2017M610696), China Scholarship Council and the International Centre for Radio Astronomy Research.

The SAMI Galaxy Survey is based on observations made at the Anglo-Australian Telescope. The Sydney-AAO Multi-object Integral field spectrograph (SAMI) was developed jointly by the University of Sydney and the Australian Astronomical Observatory. The SAMI input catalogue is based on data taken from the Sloan Digital Sky Survey, the GAMA Survey and the VST ATLAS Survey. The SAMI Galaxy Survey is supported by the Australian Research Council Centre of Excellence for All Sky Astrophysics in 3 Dimensions (ASTRO 3D), through project number CE170100013, the Australian Research Council Centre of Excellence for All-sky Astrophysics (CAASTRO), through project number CE110001020, and other participating institutions. The SAMI Galaxy Survey website is <http://sami-survey.org/>.

REFERENCES

- Ahn, C. P., Alexandroff, R., Allende Prieto, C., et al. 2012, *ApJS*, 203, 21
- Allen, J. T., Croom, S. M., Konstantopoulos, I. S., et al. 2015, *MNRAS*, 446, 1567
- Baldry, I. K., Driver, S. P., Loveday, J., et al. 2012, *MNRAS*, 421, 621
- Bland-Hawthorn, J., Bryant, J., Robertson, G., et al. 2011, *Optics Express*, 19, 2649
- Binney, J. 2005, *MNRAS*, 363, 937
- Binney J., Tremaine S. D. 1987, *Galactic Dynamics*. Princeton Univ. Press, NJ
- Brough, S., van de Sande, J., Owers, M. S., et al. 2017, *ApJ*, 844, 59
- Bryant, J. J., Bland-Hawthorn, J., Fogarty, L. M. R., Lawrence, J. S., & Croom, S. M. 2014, *MNRAS*, 438, 869
- Bryant, J. J., Owers, M. S., Robotham, A. S. G., et al. 2015, *MNRAS*, 447, 2857
- Butler, K. M., Obreschkow, D., & Oh, S.-H. 2017, *ApJ*, 834, L4
- Cappellari, M. 2002, *MNRAS*, 333, 400
- Cappellari, M., & Emsellem, E. 2004, *PASP*, 116, 138
- Cappellari, M., Emsellem, E., Bacon, R., et al. 2007, *MNRAS*, 379, 418
- Cappellari, M., McDermid, R. M., Alatalo, K., et al. 2012, *Nature*, 484, 485
- Cappellari, M., McDermid, R. M., Alatalo, K., et al. 2013, *MNRAS*, 432, 1862
- Cappellari, M. 2016, *Annual Review of Astronomy and Astrophysics*, 54, 597
- Cappellari, M. 2017, *MNRAS*, 466, 798
- Chabrier, G. 2003, *PASP*, 115, 763
- Cole, S., Lacey, C. G., Baugh, C. M., & Frenk, C. S. 2000, *MNRAS*, 319, 168
- Cole, S. 2011, *MNRAS*, 416, 739
- Cortese, L., Fogarty, L. M. R., Bekki, K., et al. 2016, *MNRAS*, 463, 170
- Cortese, L., van de Sande, J., Lagos, C. P., et al. 2019, *MNRAS*, 485, 2656
- Crain, R. A., Schaye, J., Bower, R. G., et al. 2015, *MNRAS*, 450, 1937
- Croom, S. M., Lawrence, J. S., Bland-Hawthorn, J., et al. 2012, *MNRAS*, 421, 872
- Davidzon, I., Ilbert, O., Laigle, C., et al. 2017, *A&A*, 605, A70
- Davies, L. J. M., Driver, S. P., Robotham, A. S. G., et al. 2016, *MNRAS*, 461, 458
- Driver, S. P., Allen, P. D., Liske, J., & Graham, A. W. 2007, *ApJ*, 657, L85
- Driver, S. P., Hill, D. T., Kelvin, L. S., et al. 2011, *MNRAS*, 413, 971
- Driver, S. P., Andrews, S. K., da Cunha, E., et al. 2018, *MNRAS*, 475, 2891.
- Eddington, A. S. 1913, *MNRAS*, 73, 359
- Emsellem, E., Monnet, G., & Bacon, R. 1994, *A&A*, 285, 723
- Emsellem, E., Cappellari, M., Krajnović, D., et al. 2007, *MNRAS*, 379, 401
- Emsellem, E., Cappellari, M., Krajnović, D., et al. 2011, *MNRAS*, 414, 888.
- Erwin, P., Saglia, R. P., Fabricius, M., et al. 2015, *MNRAS*, 446, 4039
- Faber, S. M., Tremaine, S., Ajhar, E. A., et al. 1997, *AJ*, 114, 1771
- Fall, S. M., & Efstathiou, G. 1980, *MNRAS*, 193, 189
- Foster, C., van de Sande, J., D'Eugenio, F., et al. 2017, *MNRAS*, 472, 966.
- Genel, S., Vogelsberger, M., Springel, V., et al. 2014, *MNRAS*, 445, 175
- Gerhard, O. E. 1981, *MNRAS*, 197, 179
- Graham, M. T., Cappellari, M., Li, H., et al. 2018, *MNRAS*, 477, 4711
- Green, A. W., Croom, S. M., Scott, N., et al. 2018, *MNRAS*, 475, 716
- Greene, J. E., Leauthaud, A., Emsellem, E., et al. 2017, *ApJ*, 851, L33.
- Greene, J. E., Leauthaud, A., Emsellem, E., et al. 2018, *ApJ*, 852, 36.
- Guo, K., Zheng, X. Z., Wang, T., et al. 2015, *ApJ*, 808, L49.
- Hernquist, L. 1992, *ApJ*, 400, 460
- Hernquist, L. 1993, *ApJ*, 409, 548
- Heyl, J. S., Hernquist, L., & Spergel, D. N. 1994, *ApJ*, 427, 165
- Ilbert, O., Salvato, M., Le Floch, E., et al. 2010, *ApJ*, 709, 644
- Jesseit, R., Cappellari, M., Naab, T., Emsellem, E., & Burkert, A. 2009, *MNRAS*, 397, 1202
- Kang, X., Macciò, A. V., & Dutton, A. A. 2013, *ApJ*, 767, 22
- Kelvin, L. S., Driver, S. P., Robotham, A. S. G., et al. 2014, *MNRAS*, 444, 1647
- Khochfar, S., Emsellem, E., Serra, P., et al. 2011, *MNRAS*, 417, 845.
- Kormendy, J., & Bender, R. 1996, *ApJ*, 464, L119
- Lagos, C. del P., Stevens, A. R. H., Bower, R. G., et al. 2018, *MNRAS*, 473, 4956
- Lagos, C. del P., Schaye, J., Bahé, Y., et al. 2018, *MNRAS*, 476, 4327.
- Lilly, S. J., & Carollo, C. M. 2016, *ApJ*, 833, 1
- Liske, J., Baldry, I. K., Driver, S. P., et al. 2015, *MNRAS*, 452, 2087.
- Macciò, A. V., Kang, X., Fontanot, F., et al. 2010, *MNRAS*, 402, 1995
- Martig, M., Bournaud, F., Croton, D. J., et al. 2012, *ApJ*, 756, 26
- Menci, N., Fiore, F., & Lamastra, A. 2012, *MNRAS*, 421, 2384
- Méndez-Abreu, J., Debattista, V. P., Corsini, E. M., & Aguerri, J. A. L. 2014, *A&A*, 572, A25
- Moffett, A. J., Ingarfield, S. A., Driver, S. P., et al. 2016, *MNRAS*, 457, 1308
- Moffett, A. J., Lange, R., Driver, S. P., et al. 2016, *MNRAS*, 462, 4336
- Naab, T., Oser, L., Emsellem, E., et al. 2014, *MNRAS*, 444, 3357
- Obreschkow, D., Murray, S. G., Robotham, A. S. G., & Westmeier, T. 2018, *MNRAS*, 474, 5500
- Peng, Y.-j., Lilly, S. J., Kovač, K., et al. 2010, *ApJ*, 721, 193
- Pillepich, A., Springel, V., Nelson, D., et al. 2018, *MNRAS*, 473, 4077
- Popesso, P., Concas, A., Morselli, L., et al. 2019, *MNRAS*, 483, 3213
- Rizzo, F., Fraternali, F., & Iorio, G. 2018, *MNRAS*, 476, 2137
- Scannapieco, C., Gadotti, D. A., Jonsson, P., et al. 2010, *MNRAS*, 407, L41
- Scott, N., Cappellari, M., Davies, R. L., et al. 2009, *MNRAS*, 398, 1835
- Scott, N., van de Sande, J., Croom, S. M., et al. 2018, *MNRAS*, 481, 2299
- Schechter, P. 1976, *ApJ*, 203, 297
- Sharp, R., Saunders, W., Smith, G., et al. 2006, *Proc. SPIE*, 6269, 62690G
- Sharp, R., Allen, J. T., Fogarty, L. M. R., et al. 2015, *MNRAS*, 446, 1551
- Tabor, M., Merrifield, M., Aragón-Salamanca, A., et al. 2017, *MNRAS*, 466, 2024
- Tabor, M., Merrifield, M., Aragón-Salamanca, A., et al. 2019, *MNRAS*, 485, 1546
- Taylor, E. N., Hopkins, A. M., Baldry, I. K., et al. 2011, *MNRAS*, 418, 1587
- Wang, L., Obreschkow, D., Lagos, C. del P., et al. 2019, *MNRAS*, 482, 5477

- Weijmans, A.-M., de Zeeuw, P. T., Emsellem, E., et al. 2014, MNRAS, 444, 3340.
- Woo, J., & Ellison, S. L. 2019, MNRAS, 487, 1927
- Wright, A. H., Robotham, A. S. G., Driver, S. P., et al. 2017, MNRAS, 470, 283
- van de Sande, J., Bland-Hawthorn, J., Fogarty, L. M. R., et al. 2017, ApJ, 835, 104
- van de Sande, J., Bland-Hawthorn, J., Brough, S., et al. 2017, MNRAS, 472, 1272.
- van de Sande, J., Scott, N., Bland-Hawthorn, J., et al. 2018, Nature Astronomy, 2, 483
- van den Bosch, F. C. 1998, ApJ, 507, 601
- Zhu, L., van de Ven, G., Méndez-Abreu, J., et al. 2018, MNRAS, 479, 945